Effects of sand and slurry characteristics on pressure infiltration of bentonite slurry into sand

TAO XU*, WAN-HUAN ZHOU†, ADAM BEZUIJEN‡, SU QIN§

*Associate Professor, School of Transportation, Southeast University, Nanjing, China, formerly Postdoctoral Fellow of University of Macau, taoxu@seu.edu.cn

†Professor, State Key Laboratory of Internet of Things for Smart City & Department of Civil and Environmental Engineering, University of Macau, Macao, hannahzhou@um.edu.mo

‡Professor, Laboratory of Geotechnics, Ghent University, Ghent, Belgium; Senior Consultant, Geo-Engineering, Deltares, Delft, the Netherlandsa, adam.bezuijen@ugent.be

§PhD student, State Key Laboratory of Internet of Things for Smart City & Department of Civil and Environmental Engineering, University of Macau, Macao, yb97412@um.edu.mo

ABSTRACT: Two series of experiments were carried out to examine pressurised bentonite slurry infiltration into saturated sand columns. Three types of sand were examined, and water–bentonite and water–bentonite–sand slurries were used in Series 1 and 2, respectively. Series 1 investigated the effect of sand particle size and Series 2 examined the effect of the fine-sand particle content in the slurry. Scanning electron microscopy (SEM) imaging was used to observe the morphological features of the dried slurry-infiltrated sand samples. A new solution for the infiltration distance during mud spurt for water–bentonite–sand slurry infiltration was verified using the data from Series 2. The infiltration test results showed that the hydraulic conductivity of the slurry-infiltrated coarse sand in Series 2 was lower than that in Series 1. Visual observations and the SEM images showed that sand particles were bound to a bentonite film, indicating that, during infiltration, the channels for fluid flow among the sand particles are

blocked by the bentonite particles adhered to the sand particles. The new solution for the infiltration distance during mud spurt for water–bentonite–sand slurry infiltration showed good agreement with the experimental results.

KEYWORDS: slurry-shield tunnelling; miniature shield machine; saturated sandy ground; ground displacement; slurry infiltration; excess pore-water pressure, tunnels & tunnelling, TBM

1. INTRODUCTION

Pressurised bentonite slurry is widely used to stabilise the tunnel face during shield tunnelling in saturated sandy soils with high water pressure. It is intended that a filter cake will be formed on the tunnel face as the slurry infiltrates into the soil. Such a filter cake is important for the stability of the tunnel face because it can transfer the slurry pressure onto the soil skeleton. Field observations of filter cake formation are difficult, and they are only possible when the excavation chamber is opened for maintenance, e.g., in the Yangtze River Tunnel in Nanjing (Fig. 1). In such conditions, a filter cake is of extreme importance for the safety of the maintenance operators. As an alternative, laboratory experiments have been widely carried out to study the mechanisms of filter cake formation (Krause, 1987; Fritz, 2007; Talmon et al., 2013; Min et al., 2013, 2019; Yin et al., 2016; Steeneken, 2016; Zizka et al., 2019; Xu and Bezuijen, 2019a, 2019b, 2019c).

Fig. 1. Filter cake formed on the tunnel face during hyperbaric intervention in the Nanjing Yangtze River Tunnel (modified after Zhu et al., 2019)

In the process of slurry infiltration, two stages are normally distinguished: mud spurt and filter cake formation. Min et al. (2013) identified criteria for filter cake formation during slurry infiltration into highly permeable soils using the ratio between the average pore size of the soil

and the bentonite particle size. Min et al. (2019) examined the effects of seawater intrusion on filter cake formation. Talmon et al. (2013) proposed using a Péclet number (*Pe*) to judge the formation of a filter cake:

$$Pe = \frac{v_p d}{c_v}, \quad (1)$$

where v_p is the pore fluid velocity, d is the hydraulic pore diameter, and c_v is the consolidation coefficient of the bentonite slurry. A value of $Pe < 10$ implies that a filter cake can be formed.

During excavation, the cutting wheel will cut off the filter cake, and this can change the infiltration conditions on the tunnel face. Xu and Bezuijen (2019b) therefore carried out a series of infiltration tests to establish the differences before and after the removal of the filter cake. It was found that the infiltration will continue once the filter cake is removed, and the final infiltration distance will be further increased. Xu and Bezuijen (2019a, 2019b, 2019c) also investigated the hydraulic conductivity of sand for slurry. It was found that the hydraulic conductivity values of Mol 32 sand (a poorly graded quartz sand with $d_{50} = 0.154$ mm and a hydraulic conductivity for water $k_s = 4 \times 10^{-4}$ m/s at relative density ≥ 90%) for slurries with an apparent viscosity of 4.5 to 7.5 mPa·s were in the range 8.0×10^{-5} to 2.0×10^{-5} m/s. However, in these tests, only the infiltration of slurry into a fine sand column was investigated. Therefore, the effect of the particle size in the sand column on slurry infiltration is the first topic of this paper.

In the above experiments, clean slurry made from bentonite and water was used. However, as reported by COB (2000), the density of the slurry in the excavation chamber ranged between 1260 and 1450 kg/m^3. In other words, rather than clean slurry, slurry containing soil will be present in the gap between the cutter head and the tunnel face. This means that the infiltrating slurry will contain soil particles. Xu and Bezuijen (2019b) therefore conducted experiments

examining the infiltration of slurry containing fine sand particles into saturated fine sand. The experimental results showed that there will be no external filter cake formed on the sand surface with a high-density slurry ($\geq$ 1300 kg/m^3). Moreover, a higher density (more sand in the slurry) leads to a larger infiltration distance. This is because more sand particles in the slurry will be deposited on the interface between the slurry and the sand column, meaning that more bentonite particles will adhere to these deposited sand particles. According to Xu and Bezuijen (2019b), a slurry with a higher bentonite content leads to a smaller infiltration distance. In their experiments, only fine sand was used to make the sand column. When coarse sand is used, fine sand particles may also travel with the infiltrating slurry into the pores. The effects of the fine sand-particle content of the slurry on its infiltration have not been investigated, and this is therefore the second topic of this paper.

To address these issues, two series of experiments were performed to examine the pressure infiltration of bentonite slurry into sands with various particle sizes. Series 1 aimed to examine the effect of the particle size on filter cake formation. Series 2 examined the infiltration behaviour of slurry containing fine sand particles into sand. Scanning electron microscopy (SEM) imaging was conducted to observe the morphological features of the dried slurry-infiltrated sand samples. Through analysis of the experimental results, new findings relating to the pressure infiltration of slurry under various conditions were obtained.

2. MATERIALS AND METHODS

2.1. Materials

Three grades were sieved from China standard sand (Pingtan sand) to make the samples: fine sand (FS), medium sand (MS), and coarse sand (CS). The particle-size distribution (PSD) of the source sand, along with the boundaries indicating the grades, is plotted in Fig. 2. The properties of the three types of sand are summarised in Table 1. The hydraulic conductivity

values were determined using constant-head permeability tests, and these correspond to a relative density of 90%.

Table 1. Properties of the three sand grades

Type	Particle size (mm)	Relative density (%)	Porosity	Hydraulic conductivity value for water (m/s)
FS	< 0.425	90	0.40	0.0017
MS	[0.425, 1)	90	0.41	0.0276
CS	[1, 4)	90	0.41	0.0570

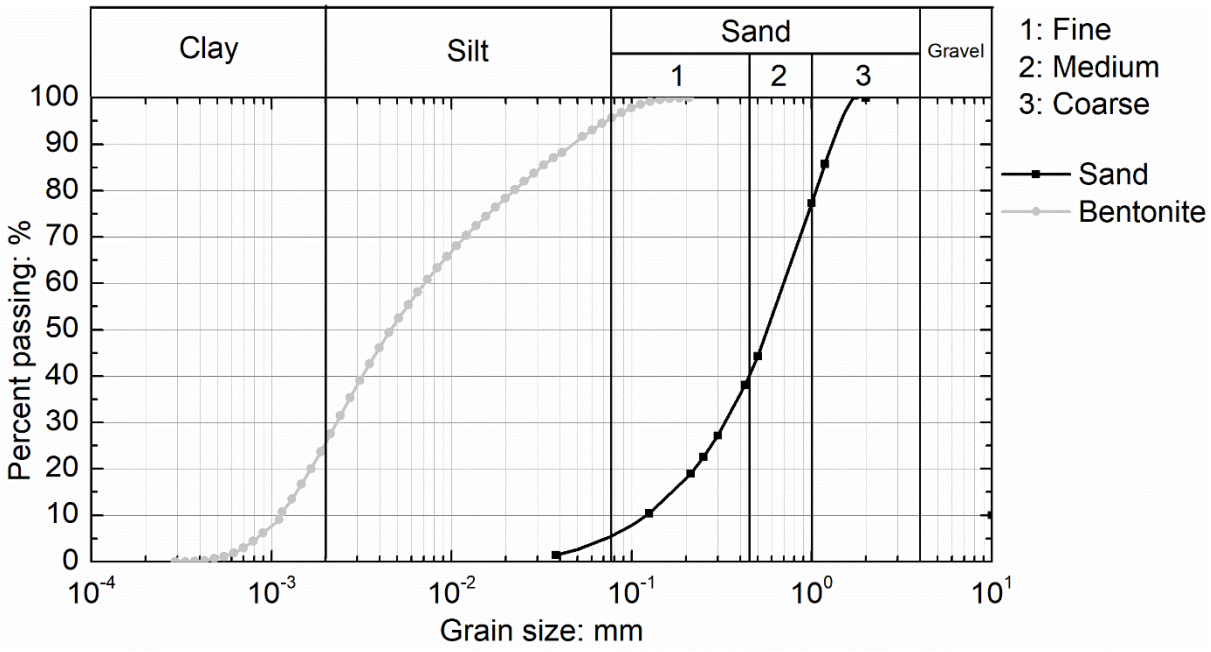

Fig. 2. Particle-size distributions of the used sand and bentonite

A commercial sodium bentonite was used to prepare the slurry, the PSD of which is also plotted in Fig. 2. The PSD of the bentonite was measured using a Malvern Mastersizer 3000 particle-size analyser using a wet sample, and the PSD of the sand was measured in sieves using a dry sample. The mineral contents of the bentonite are shown in Table 2. A Hamilton Beach HMD200 mixer was used to mix the bentonite with water at 12 000 rpm for 20 min, and this

was hydrated for 24 h, as specified by the API (2003). Four commonly used concentrations – 40, 50, 60, and 70 g/l (bentonite/water) – were adopted for the experiments. Before use, the hydrated slurry was mixed again at 12 000 rpm for 5 min, using the same mixer. The shear stresses under various shear rates for the slurries with different bentonite concentrations were determined using a Fann RheoVADR digital rheometer (see Table 3). Data points were obtained for 3, 6, 100, 200, 300, and 600 rpm, corresponding to shear rates between 5.1 and 1021 s^{-1}. Table 4 shows the rheological properties determined using the rheological curve shown in Fig. 3.

Table 2. Mineral contents of the used bentonite

Mineral composition	Content (%)
$Al_{2.9}Fe_{0.04}H_2K_{0.86}Mg_{0.06}Na_{0.1}O_{12}Si_3$	22
$Na_{0.499}Ca_{0.491}(Al_{1.488}Si_{2.506}O_8)$	19
$Na_{9.9}K_{3.46}Ca_{3.52}Al_{15.9}Si_{56.1}O_{144}(H_2O)_{44.68}$	15
$Al_3CaH_{10}KO_{17}Si_3$	14
SiO_2	11
$Al_2Si_4O_{10}(OH)$	10
$Al2(Si_2O_5)(OH)_4$	9

Table 3. Shear stresses (Pa) from the rheometer for various bentonite concentrations

Shear speed (rpm) / Bentonite concentration (g/l)	3	6	100	200	300	600
40	1.6	1.8	7.0	9.9	12.2	18.0
50	1.8	1.9	8.8	12.0	14.6	21.9
60	4.0	4.1	9.1	12.9	15.8	23.3
70	9.4	9.6	21.4	28.1	33.5	46.4

Table 4. Rheological properties of slurries with various bentonite concentrations

Bentonite concentration (g/l)	Apparent viscosity (mPa·s)	Plastic viscosity (mPa·s)	Yield point (Pa)	Yield strength (Pa)
40	17.6	5.7	6.4	1.6
50	21.4	7.2	7.3	1.8
60	22.8	7.4	8.3	4.1
70	45.4	12.7	20.6	9.4

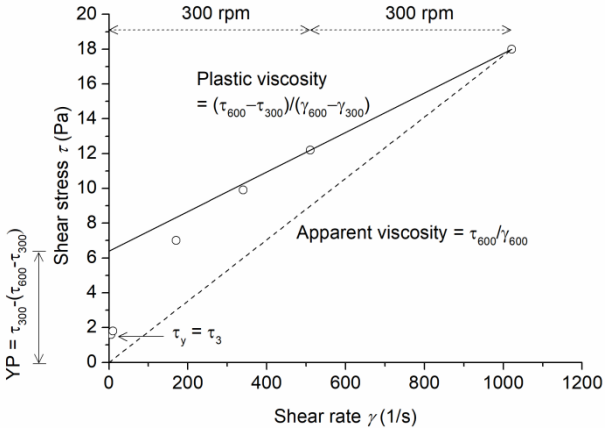

Fig. 3. Interpretation of data from a rheometer test for a bentonite concentration of 40 g/l

A value of 60 g/l was adopted as the bentonite concentration of the basic water–bentonite slurry due to the minimum yield strength requirement for suspending the sand. This was estimated using:

$$\tau_{\mathrm{f}} = 0.7\frac{2}{3\pi} d_{\mathrm{s}} \left(\gamma_{\mathrm{s}} - \gamma_{\mathrm{b}}\right), \tag{2}$$

where d_s and γ_s are the mean diameter and specific weight of the sand particles, respectively, and γ_b is the specific weight of the bentonite slurry (datasheet; Leutert, 2016). This formula was used for the experiments by Xu and Bezuijen (2019b). For the fine sand (mean diameter 190 μm), the required minimum shear strength of the slurry is 0.5 Pa. In this study, all the bentonite concentrations met this requirement (see Table 4). As a slurry with a low bentonite

concentration will lead to a very deep infiltration, the amount of slurry added to the experimental system may be insufficient. A relatively high bentonite concentration (60 g/l) was therefore adopted in the tests of Series 2.

2.2. Experimental equipment and procedure

The details of the experimental equipment and procedure are as described by Xu and Bezuijen (2019a, 2019b). This system imposes flow velocities that are comparable to what could be expected at the front of a 6-m-diameter slurry shield (~2×10^{-5} to 5×10^{-3} m/s). Herein, only the modifications to the system are described. As Fig. 4 shows, in the modified system, the poly(methyl methacrylate) cylinder consists of two parts that are connected by a flange. This makes it possible to extract the slurry-infiltrated sand sample from the apparatus.

In the experimental procedure, a porous stone is placed beneath the small cylinder at the bottom of the lower cylinder, and this allows water to flow but blocks the movement of sand particles. The lower cylinder is filled to the top with sand to a total length of 350 mm, including 50 mm in the small cylinder. A 300-mm-thick layer of slurry is then poured into the upper cylinder onto the surface of the sand column. According to Xu and Bezuijen (2019a), the equivalent length of a homogeneous sand column is:

$$L_s = L_{s1} + L_{s2}\left(\frac{D_1}{D_2}\right)^2 + \frac{D_1^2}{4D_2} - \frac{D_1}{4}, \tag{3}$$

where L_{s1} (L_{s2}) is the length of sand column in the large (small) cylinder, and D_1 (D_2) is the inner diameter of the large (small) cylinder. For an applied air pressure of 50 kPa, the hydraulic gradient over the sand sample in this system is $i = \Delta\varphi/L_s = 5.0$ m/3.6 m ≈ 1.4.

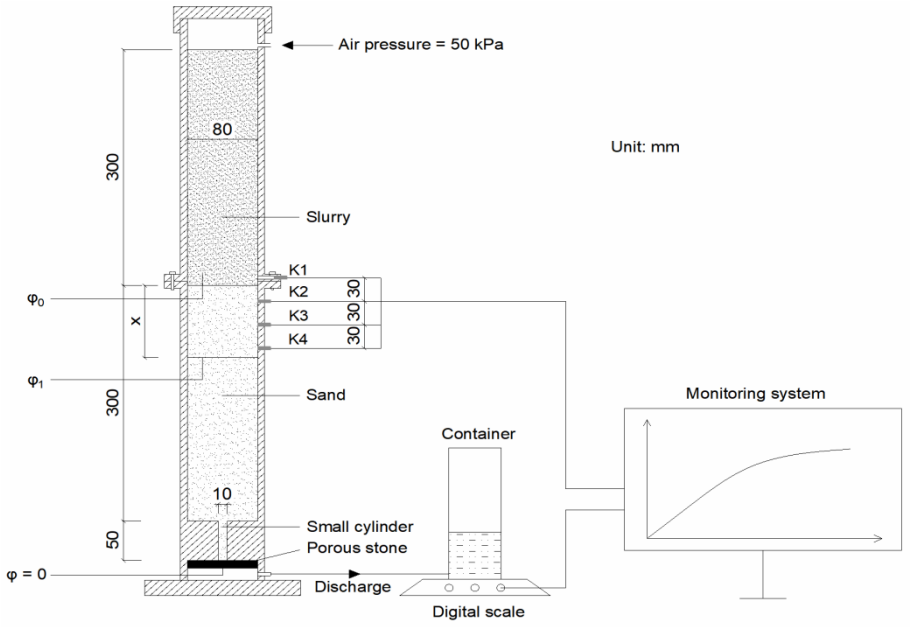

Fig. 4. Schematic of the apparatus for infiltration tests: *x* is the infiltration distance at any time, φ is the piezometric head at the outlet, φ_0 is the piezometric head at the surface of the sand column, and φ_1 is the piezometric head at the place where the slurry front reaches

Four VJ Tech VJT0250 pore-water pressure transducers (PPTs) with a pressure range of 0 to 1 MPa were installed in the taps on the cylinder to measure the pore-water pressure in the slurry and the sand. The PPT labelled K1 was positioned 10 mm above the slurry–sand interface, while K2, K3, and K4 were located at 20, 50, and 80 mm below the slurry–sand interface, respectively.

In Series 2, after making the same 60 g/l bentonite slurry as in Series 1, fine sand (<0.425 mm) was added to the slurry and mixed in a low-speed mixer for 5 min. The amounts of slurry and sand for the four densities of slurry are summarised in Table 5. Each test lasted 1 h (corresponding to the excavation time for a single ring) and was started by opening the water-discharge valve. Throughout the tests, the amount of discharged water was measured continuously with an electronic balance, and the pore-water pressures at different depths were measured once every second using the PPTs. After each test, the flange was loosened, and the

remaining slurry was removed. A thin-walled steel cylinder with an inner diameter of 38 mm was used to penetrate the slurry-infiltrated sand, and a 100-mm-thick sand sample was extracted. This sample was then divided into five 20-mm-thick sections (Fig. 5). The water content of each piece was determined by drying it in an oven at 105°C.

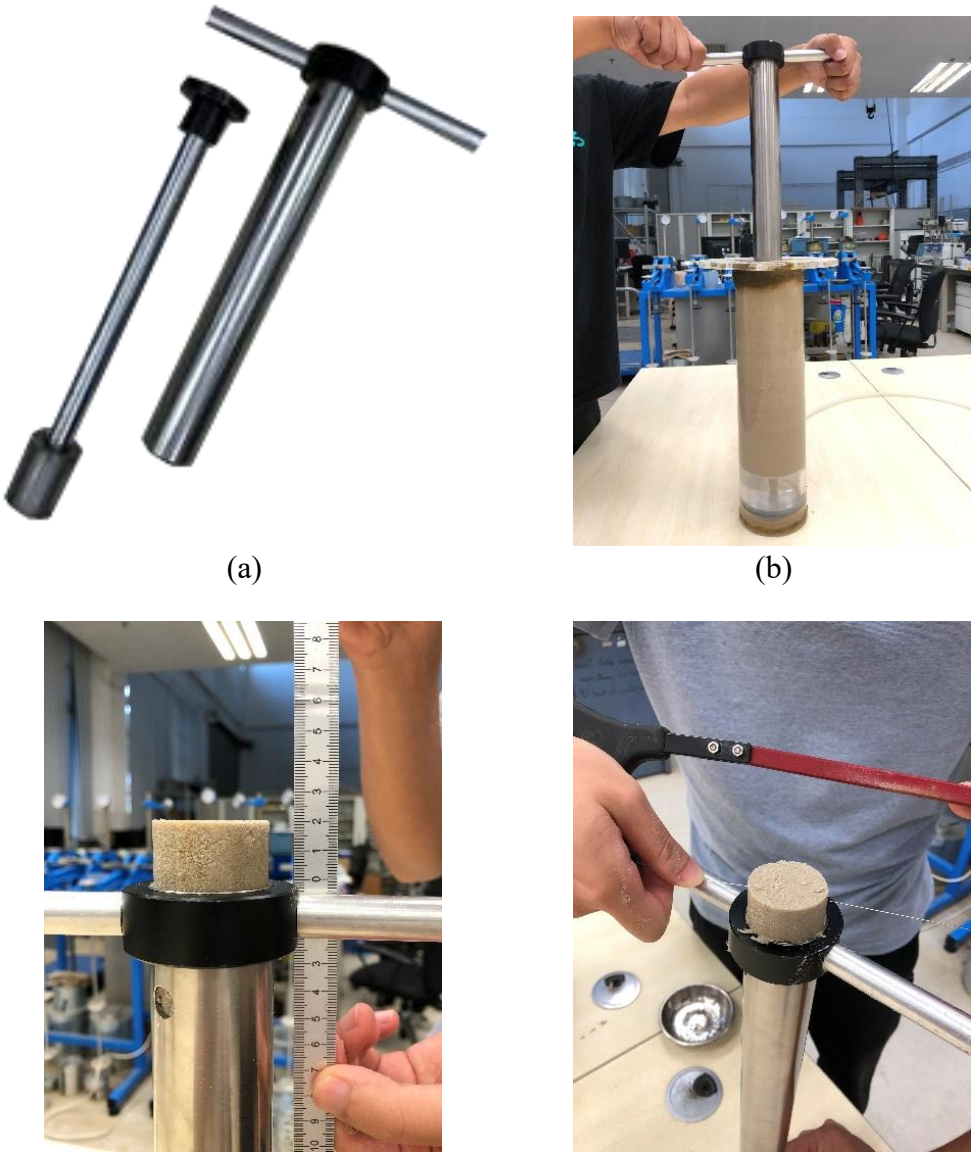

(a) (b)

(c) (d)

Fig. 5. Procedure for sampling the slurry-infiltrated sand: (a) thin-walled steel cylinder penetration device; (b) penetrating the sand and extracting the sample; (c) pushing out the sample; (d) cutting off a 20-mm-thick sample

175 **Table 5. Proportions of slurry mixture components**

Test No.	Density (kg/m^3)	Water (kg)	Bentonite (kg)	Sand (kg)
FS/MS/CS-40	1025	1000	40	0
FS/MS/CS-50	1031	1000	50	0
FS/MS/CS-60	1037	1000	60	0
FS/MS/CS-70	1041	1000	70	0
CS-1037	1037	1000	60	0
CS-1100	1100	1000	60	110
CS-1300	1300	1000	60	530
CS-1500	1500	1000	60	1090

176

177 ## 3. EXPERIMENTAL RESULTS

178 ### *3.1. Infiltration distance*

179 #### 3.1.1. Water–bentonite slurry

180 Figure 6 shows the infiltration distances against the square root of time, measured during Series
181 1, for the different sand types and bentonite concentrations. The actual infiltration distance was
182 not directly measured; instead, the infiltration distance x was calculated using the measured
183 volume of the water discharged from the sand column:

184 $$x = \frac{V}{n \cdot A}, \tag{4}$$

185 where V is the water volume discharged from the sand column, n is the porosity of the saturated
186 sand, and A is the cross-sectional area of the sand column in the large-diameter cylinder. The
187 final infiltration distance is the calculated value after 1 h of infiltration. The calculated values
188 are slightly larger than the observed values. According to Xu and Bezuijen (2019), ‘infiltration’
189 is defined as the replacement of the original pore water with the slurry (water and bentonite

particles) rather than the visually observed slurry front; the water front moves somewhat faster than the slurry front, and the latter will thus be behind than the former.

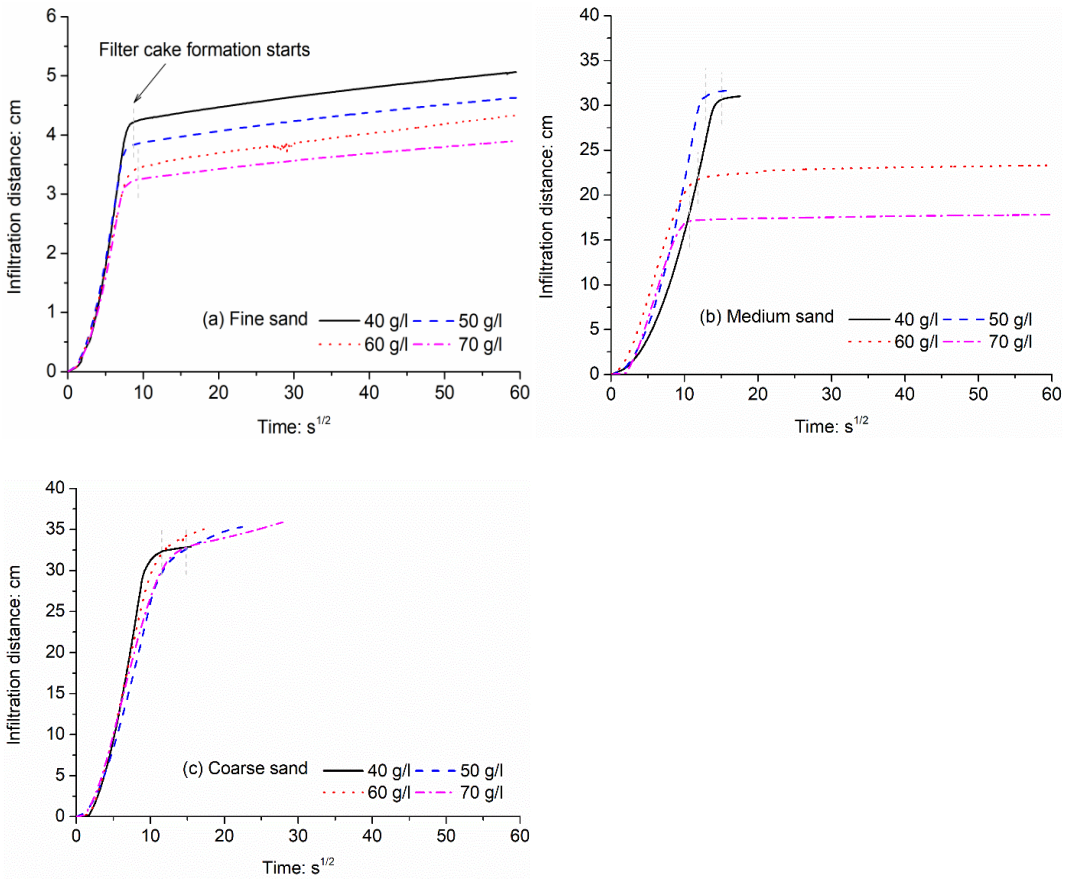

Fig. 6. Infiltration distance against the square root of time for the different sand types and bentonite concentrations

For tests FS-40, FS-50, FS-60, FS-70, MS-60, and MS-70, the mud spurt and filter cake formation stages were clearly distinguishable. For tests MS-40, MS-50, CS-40, CS-50, CS-60, and CS-70, most slurry had infiltrated into the sand within 15 min. For these cases, each test was stopped once all the slurry had infiltrated into the sand. With a longer sand column and more slurry, the infiltration distances are expected to be longer. It appears that the infiltration distance decreases with the bentonite concentration for the fine and medium sand. For the coarse sand, the infiltration distances within 100 s were almost the same for different bentonite

concentrations because the total flow resistance during mud spurt is dominated by the flow resistance for the out flowing water of the small cylinder. When filter cake formation starts, the flow resistance of the cake becomes dominant. Furthermore, greater infiltration distances were observed for the medium and coarse sands than for the fine sand.

From Fig. 7, it can be seen that the amount of bentonite that reached the layer 20 mm below the surface of the fine sand was limited. The top 20-mm sample taken from the fine sand stood like a soil block (upper left sample in Fig. 7a), but the samples from greater depths (20 to 100 mm) collapsed. It seems that the interparticle interactions beyond a depth of 20 mm were not enhanced by the bentonite. For the medium and coarse sands, the samples from both the surface (top 20 mm) and greater depths (20 to 100 mm) stood like soil blocks. This indicates that, even below 20 mm, the sand particles were bound to the bentonite.

Figures 8 and 9 contain SEM images showing the microscale structures of the dry slurry-infiltrated sand. These indicate that the individual sand particles are bound by the bentonite film. Clearly, during infiltration, some of the channels between the sand particles will become blocked by the bentonite particles. A comparison between the water-content values of the slurry-infiltrated sand gives additional evidence for this. As Fig. 10 shows, the water-content values of the fine sand at depths from 20 to 100 mm are greater than those for the medium and coarse sands. In all cases, the water-content value is greater for the top layer (0 to 20 mm) because the surface filter cake has not been removed and the amount of water inside it is relatively large. This indicates that the void ratio of the slurry-infiltrated fine sand is larger than those of the slurry-infiltrated medium and coarse sands; the bentonite particles infiltrate further into the pores of the medium and coarse sands than those of the fine sand.

(a)

(b)

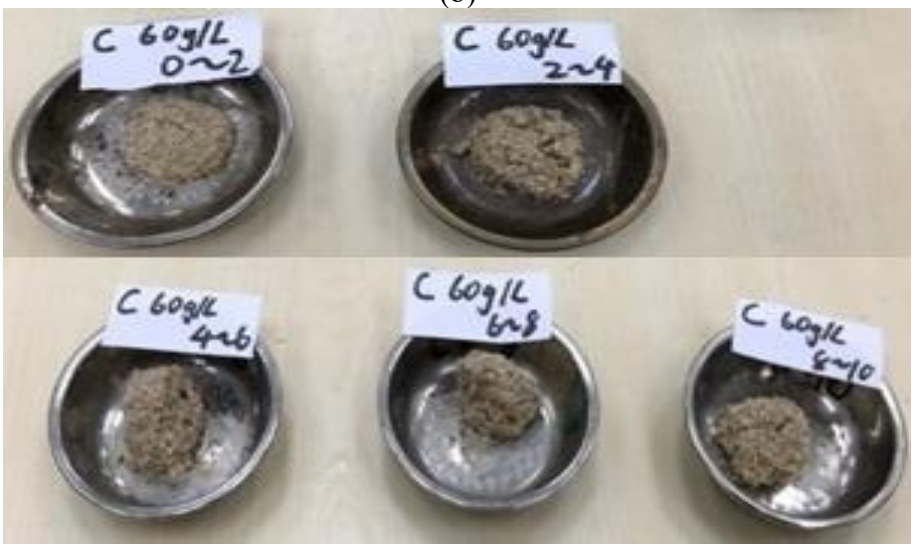

(c)

Fig. 7. Samples of slurry-infiltrated sand taken from the tests with 60 g/l water–bentonite slurry: (a) FS; (b) MS; (c) CS

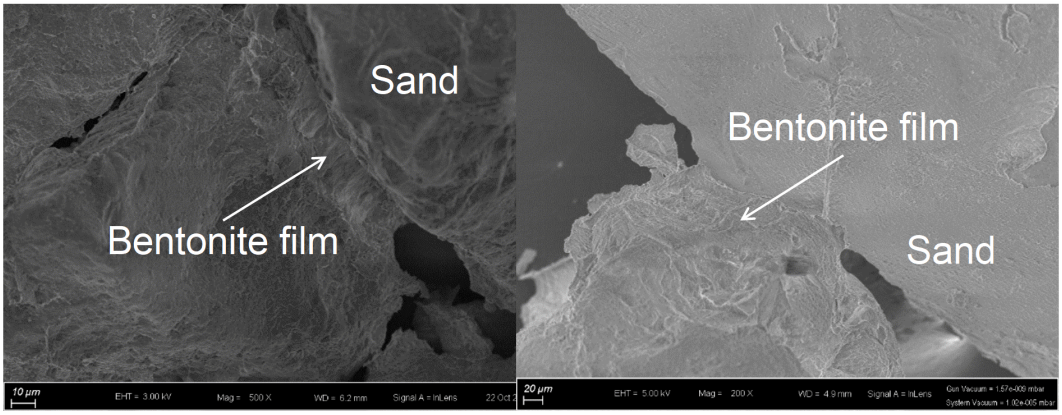

233

234 **Fig. 8. SEM images of dried slurry-infiltrated sand (water–bentonite slurry)**

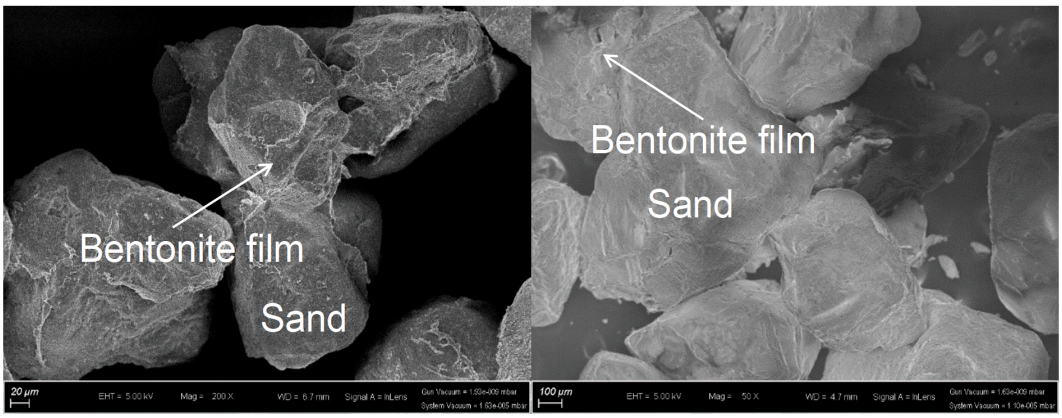

235

236 **Fig. 9. SEM images of dried slurry-infiltrated sand (water–bentonite–sand slurry)**

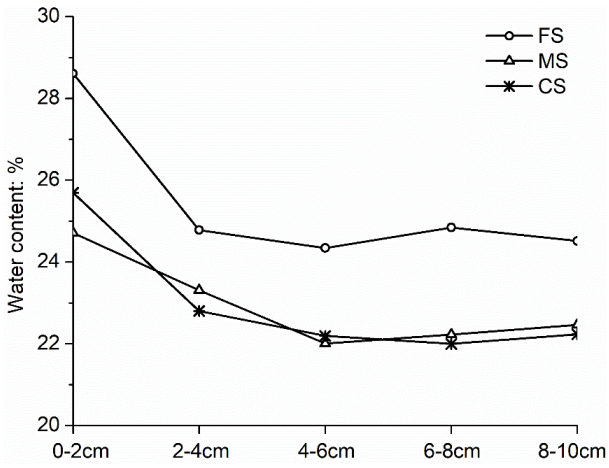

237

238 **Fig. 10. Water-content values of slurry-infiltrated sand at various depths for different**

239 **sand types (60 g/l water–bentonite slurry)**

3.1.2. Water–bentonite–sand slurry

Fig. 11 shows the infiltration distances for the infiltration of water–bentonite–sand slurry into the coarse sand column. It was found that no filter cake was formed for a high slurry density (≥1300 kg/m^3). This is comparable to the result of water–bentonite–sand slurry infiltration into fine sand reported by Xu and Bezuijen (2019b). The data in Fig. 11 can also be used to plot the flow velocity, as shown in Fig. 12. The flow velocity during infiltration of the water–bentonite slurry was faster than that of the water–bentonite–sand slurry. When a filter cake is formed, the flow velocity is extremely slow and decrease with the square root of time. Compared to the water–bentonite slurry, the additional sand particles in the water–bentonite–sand slurry will be embedded in the filter cake and hence the flow resistance will be larger. Therefore, the infiltration velocity for the water–bentonite slurry was found to be greater than that for the water–bentonite–sand slurry.

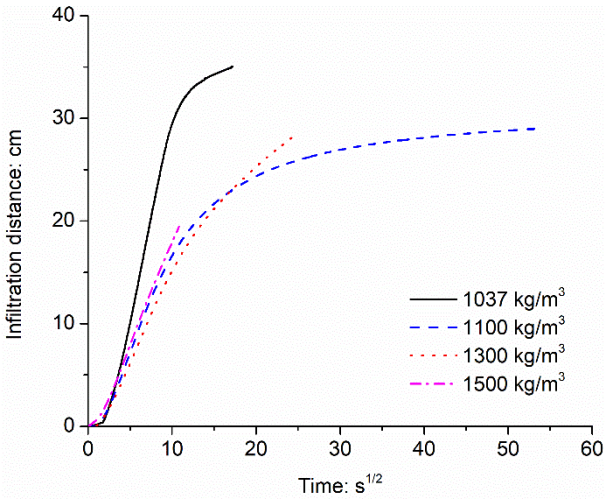

Fig. 11. Infiltration distances into coarse sand against the square root of time for slurries of various densities containing fine sand

After test CS-1300, the mixture remaining on the sand surface was taken out and washed using pure water, and this was then dried for 24 h at 105°C in an oven. It was found that 56% of the

weight of the fine sand added to the slurry had been lost. This means that the fine sand particles did indeed travel with the infiltrating slurry into the pores of the sand column. This is in contrast to the results of Xu and Bezuijen (2019b), because in their experiments the sand particles in the slurry had the same diameter as the sand particles of the sand column, and infiltration of the sand particles from the slurry into the sand column was thus not possible. This phenomenon was not captured in the SEM tests; further evidence is still needed.

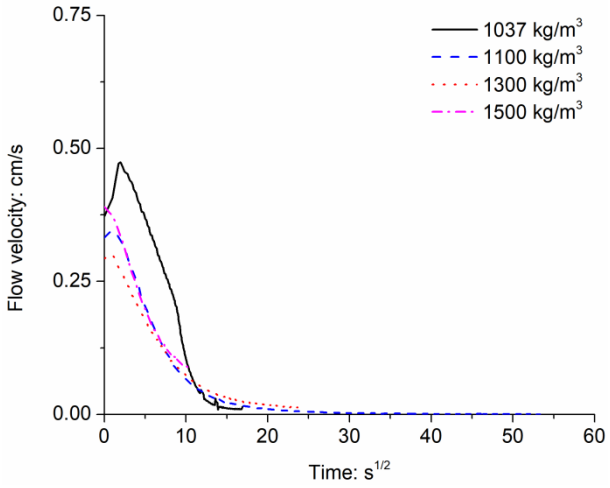

Fig. 12. Flow velocities in the coarse sand against the square root of time for slurries of various densities containing fine sand

3.2. Hydraulic conductivity of sand for slurry

The local hydraulic conductivity value of sand for slurry can be determined from the measured flow rate under set flow conditions using Darcy's law:

$$k_b = \frac{\Delta L_s Q}{(\Delta p' / \gamma_b) A}, \tag{5}$$

where ΔL_s is the thickness of sand between two adjacent PPTs, Q is the discharge, $\Delta p'$ is the corresponding difference in pore pressure over the sand between two adjacent PPTs, γ_b is the

specific weight of the slurry, and A is the cross-sectional area of the sand column in the large-diameter cylinder.

The difference in pore-water pressure over two adjacent PPTs (K1–K2, K2–K3, or K3–K4) can be obtained from the measurements. For example, Fig. 13 shows the difference in pore-water pressure for the test FS-60. The thicknesses of the sand between K1 and K2, K2 and K3, and K3 and K4 are 20, 30, and 30 mm, respectively. The cross-sectional area of the sand column the large-diameter cylinder is 5027 mm^2. The values of Q can be derived from Figs. 6 and 11. The hydraulic conductivity values can then be calculated from equation (5).

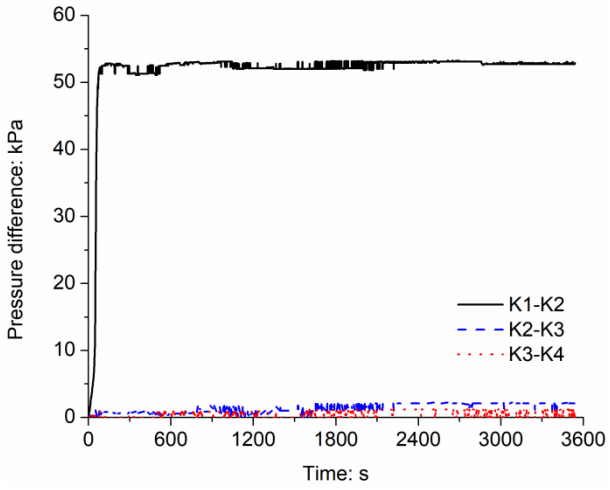

Fig. 13. Pressure differences between pairs of PPTs with infiltration distance (FS-60)

Fig.14 shows the hydraulic conductivity values of the fine sand for slurries with various bentonite concentrations. During mud spurt, the arithmetic mean value of the hydraulic conductivities was between 2.0×10^{-6} and 2.0×10^{-5} m/s, which is comparable to the results obtained by Xu and Bezuijen (2019a, 2019b, 2019c). This period is less than 2 min. Within this time, the infiltration distance accounted for more than 90% of the final infiltration distance. From Figs. 15 and 16, it can be seen that, during mud spurt, the arithmetic mean values of the hydraulic conductivities were approximately 1.5×10^{-5} to 6.0×10^{-5} m/s and 6.0×10^{-5} to

4.0×10^{-4} m/s for the medium and coarse sands, respectively. Once a filter cake was formed, the hydraulic conductivity value close to the sand surface rapidly dropped to less than 10^{-7} m/s for all tests.

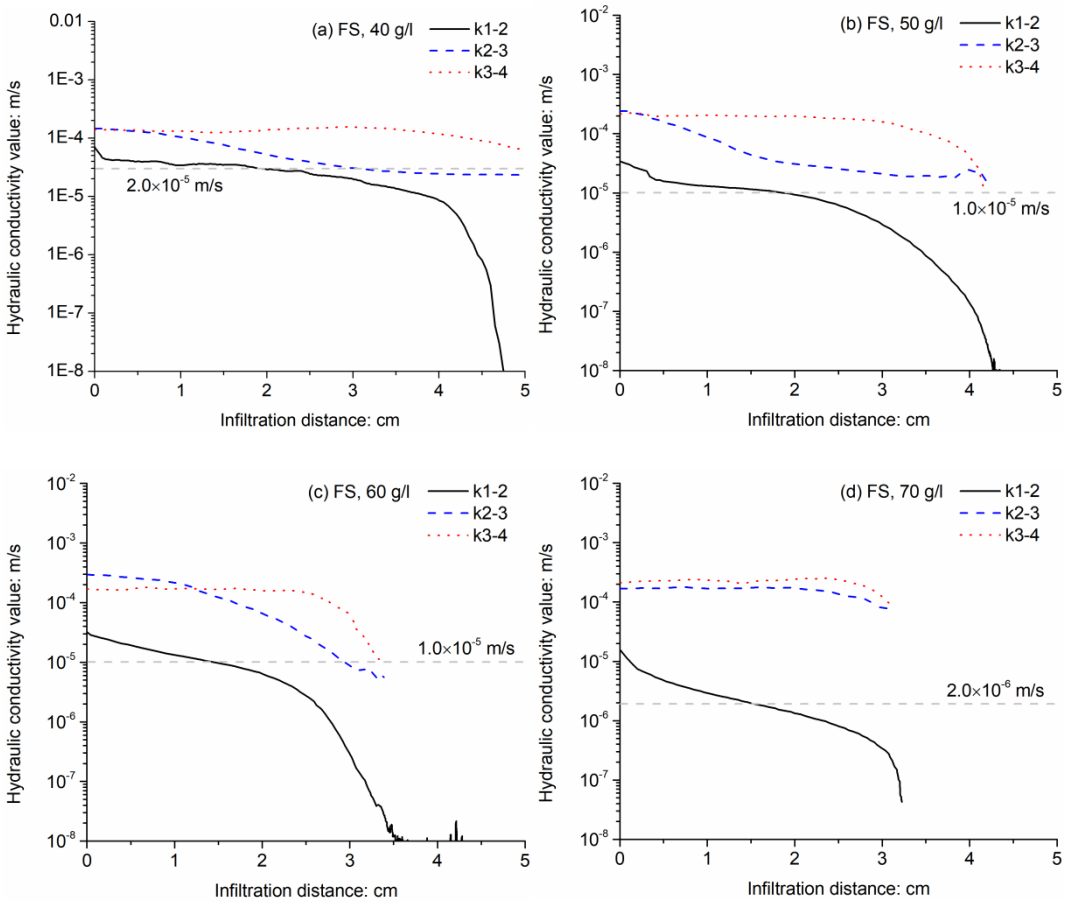

Fig. 14. Hydraulic conductivity values of the fine sand for slurries with different bentonite concentrations

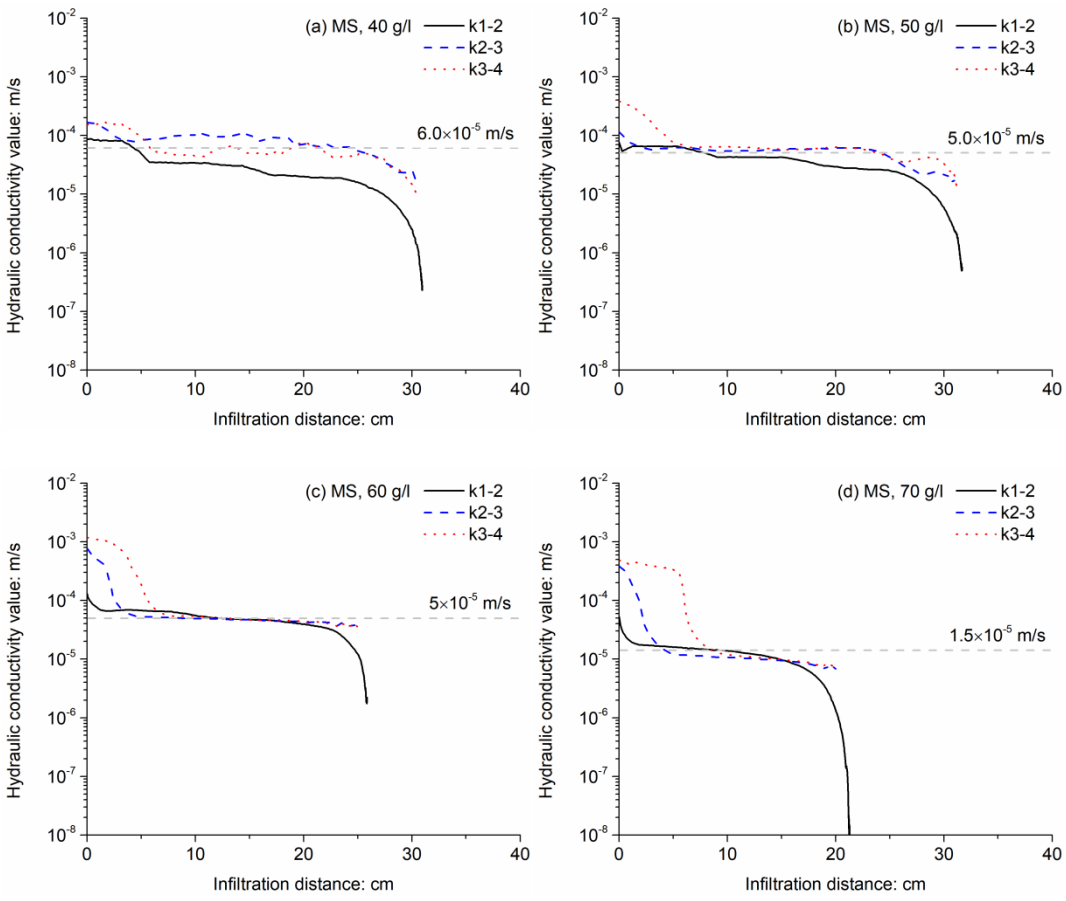

Fig. 15. Hydraulic conductivity values of the medium sand for slurries with various bentonite concentrations

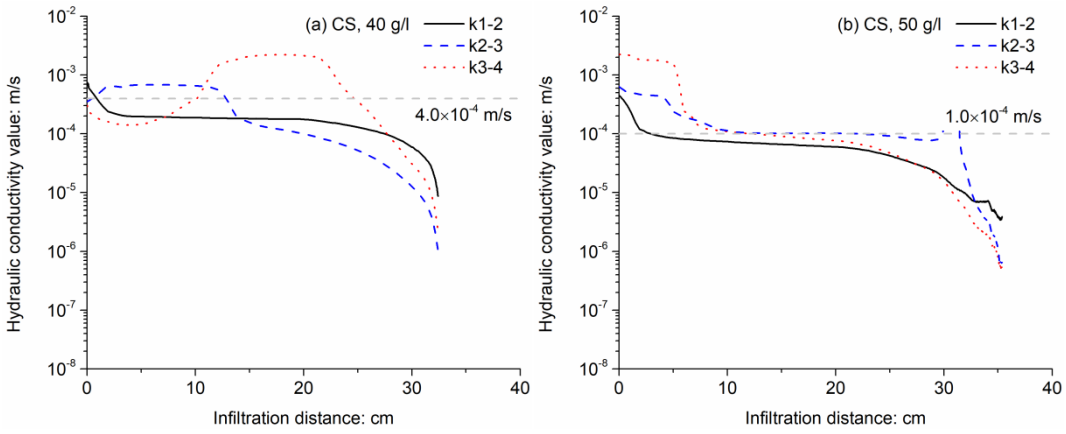

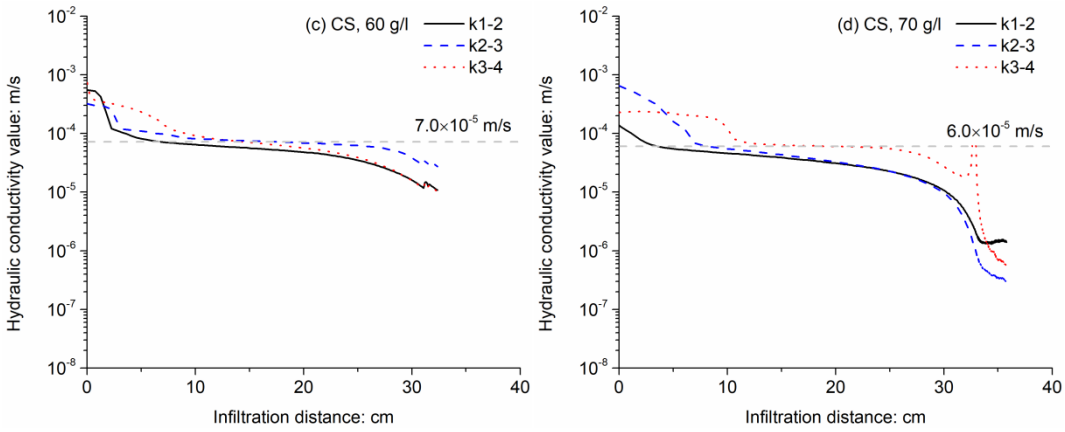

Fig. 16. Hydraulic conductivity values of the coarse sand for slurries with various bentonite concentrations

The hydraulic conductivity values of the coarse sand for slurries of various densities are plotted in Fig. 17. Fluctuations in the curves may have been caused by measurement errors in the discharge or pressure; at the stage, the discharge and pressure changes are extremely small, and errors may thus occur. For water–bentonite–sand slurry, the hydraulic conductivity decreases gradually with the infiltration. Compared to the sand infiltrated by the water–bentonite slurry, a lower hydraulic conductivity was found for the sand infiltrated by the water–bentonite–sand slurry. This indicates that, in a coarse sand, the fine sand particles infiltrating with the slurry reduce the hydraulic conductivity of sand on the tunnel face during tunnelling.

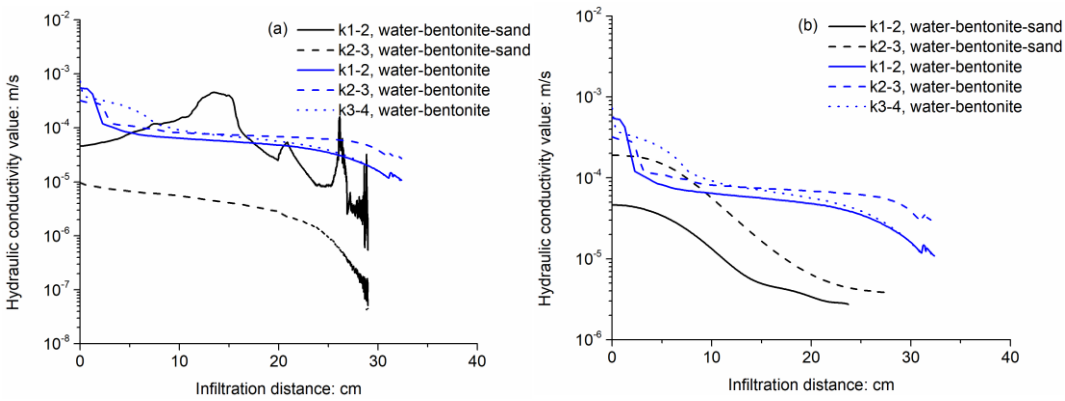

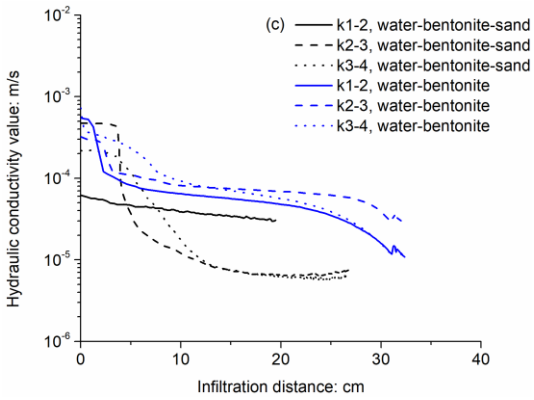

Fig. 17. Comparison of hydraulic conductivity values of coarse sand for water–bentonite slurry (1037 kg/m^3) and water–bentonite–sand slurries with various densities: (a) 1100 kg/m^3; (b) 1300 kg/m^3; (c) 1500 kg/m^3

3.3. New solution of infiltration distance during mud spurt for water–bentonite–sand slurry

Xu and Bezuijen (2019b) proposed a formula to predict the infiltration distance against time for the infiltration of water–bentonite slurry:

$$\frac{\mathrm{d}x}{\mathrm{d}t} = \frac{\varphi_0 k_\mathrm{s}}{n} \frac{1-\dfrac{x}{L}}{L_\mathrm{s} + \dfrac{k_\mathrm{s}}{k_\mathrm{b}} x}, \tag{6}$$

where x is the infiltration distance at any time (t), φ_0 is the piezometric head at the surface of the sand column, k_s is the hydraulic conductivity of sand for water, n is the porosity of the sand, x is the infiltration distance at any time, L is the maximum infiltration distance, L_s is the equivalent length of the sand column, and k_b is the hydraulic conductivity of sand for the bentonite slurry. For the boundary condition $x = 0$ at $t = 0$, this leads to:

$$t = -\frac{nL}{\varphi_0}\left[\left(\frac{L_\mathrm{s}-L}{k_\mathrm{s}} + \frac{L}{k_\mathrm{b}}\right)\ln\left(1-\frac{x}{L}\right) + x\left(\frac{1}{k_\mathrm{b}} - \frac{1}{k_\mathrm{s}}\right)\right]. \tag{7}$$

327 It is noted that the maximum infiltration distance (L) has to be determined by an infiltration test
328 rather than using the formula proposed by Krause (1987):

$$L = \frac{\Delta p d_{10}}{\alpha \tau_{\mathrm{y}}}, \tag{8}$$

329

330 where Δp is the pressure drop over the sand column, d_{10} is the grain diameter at the point in the
331 PSD at which 10% of the grains are finer than this diameter, α is a fitting factor ($2 \leq \alpha \leq 4$), and
332 τ_{y} is the yield strength of the slurry.

333 The maximum infiltration distance is determined by the yield strength of the slurry and the
334 diameter of the channel for slurry flow. Although Krause (1987) proposed a formula to predict
335 the infiltration distance, this does not consider the effect of filter cake formation. Talmon et al.
336 (2013) and Xu and Bezuijen (2019b, 2019c) showed that the maximum infiltration distance
337 calculated using equation (8) is considerably larger that the measured infiltration distance. A
338 better formula is thus needed to accurately predict the maximum infiltration distance with
339 consideration of the filter cake.

340 Xu and Bezuijen (2019b) showed that for a high-density slurry containing sand particles, there
341 is no apparent maximum infiltration distance within 1 h. Equation (7) was proposed for the
342 infiltration with the formation of an external filter cake, and it therefore cannot be used to
343 estimate the infiltration distance for water–bentonite–sand slurry.

344 Recently, Bezuijen (2019) proposed a formula to describe the infiltration of water–bentonite–
345 sand slurry for a situation in which there is no maximum infiltration depth:

$$\frac{\mathrm{d}x}{\mathrm{d}t} = \frac{\varphi_0 k_{\mathrm{s}}}{n} \frac{1}{L_{\mathrm{s}} + \frac{k_{\mathrm{s}}}{k_{\mathrm{b}}} x}, \tag{9}$$

346

This formula is the same as equation (6), but it assumes that $x \ll L$. For the boundary condition $x = 0$ at $t = 0$, this results in:

$$x = \frac{L_s k_b}{k_s}\left(\sqrt{1 + 2\frac{k_s^{\,2}}{k_b n L_s^{\,2}}\varphi_0 t} - 1\right), \tag{10}$$

Table 6 gives the values of the input parameters for the infiltration tests of 1500 kg/m^3 water–bentonite–sand slurry into coarse sand (Case 1, this study) and the infiltration tests of 1500 kg/m^3 water–bentonite–sand slurry into fine sand (Case 2, Xu and Bezuijen 2019b). The values of k_b are assumed to be the arithmetic mean values of hydraulic conductivity for slurry. Fig. 18 shows that the calculated results match the experimental results well for both cases. In this figure, the infiltration distances were calculated from the water discharge. Visual observations of the slurry showed slightly less infiltration. This calculation was made for two model tests, but it can nonetheless be directly compared with the results from a real tunnel because the pressure gradients in the soil are similar.

Table 6. Values of input parameters for the new solution of infiltration distance during mud spurt

Parameter	L_s (m)	k_b (m/s)	k_s (m/s)	n (-)	φ_0 (m)
Case 1	3.6	2.0×10^{-5}	5.7×10^{-2}	0.41	5
Case 2	3.0	1.0×10^{-6}	3.0×10^{-4}	0.37	5

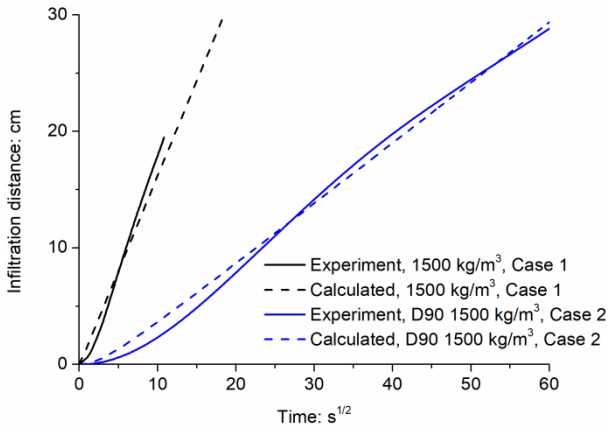

362

363 **Fig. 18. Comparison of experimental and calculated results for the infiltration distance**
364 **against time for water–bentonite–sand slurry**

365 **4. CONCLUSIONS**

366 A small modification was made to the experimental system used by Xu and Bezuijen (2019a,
367 2019b) to allow the slurry-infiltrated sand to be easily removed for visual observation and SEM
368 imaging. Two series of experiments on bentonite slurry infiltration into saturated sands were
369 conducted using this modified system. Series 1 and 2 were carried out with water–bentonite
370 slurry and water–bentonite–sand slurry, respectively. A new solution proposed by Bezuijen
371 (2019) was used to predict the infiltration distance during mud spurt for the water–bentonite–
372 sand slurry as a function of time. From analysis of the experimental results and the microscale
373 structures of the dried slurry-infiltrated sand, the following conclusions can be drawn.

374 For infiltration of water–bentonite slurry into fine sand, the external filter cake formed on the
375 sand surface impedes the infiltration into the deeper sand layer. As a result, the slurry-infiltrated
376 layer that is formed in front of the tunnel face is extremely thin, only approximately 20 mm.
377 This is dangerous for the tunnel face because a filter cake with such a thin slurry-infiltrated
378 layer is vulnerable to damage when considering the cutting depth of the cutting tools (Zizka,
379 2019). For infiltration of water–bentonite slurry into medium and coarse sands, the hydraulic

conductivity of sand for slurry is also significantly reduced, but the infiltration distance is much greater, reaching about 300 mm in 1 h.

For infiltration of water–bentonite–sand slurry into coarse sand, the infiltration distance is comparable to the results of the infiltration of water–bentonite slurry. Additional sand particles in the water–bentonite–sand slurry will be embedded in the filter cake, leading to a lower hydraulic conductivity of the filter cake for slurry.

In the SEM images, a bentonite film can be seen among the sand particles, and the sand particles are tightly bound to this bentonite film. This indicates that some of the channels for fluid flow in the sand are blocked by the bentonite particles adhered to the sand particles, and the hydraulic conductivity of the sand for slurry is thus reduced.

The new solution for the infiltration distance during mud spurt proposed by Bezuijen (2019) matches the experimental results well for the infiltration of water–bentonite–sand slurry in cases where there is no maximum infiltration depth within the limits of the experiment or the limits of ring building in a real tunnel.

ACKNOWLEDGEMENT

The financial supports provided by the Science and Technology Development Fund, Macau SAR (File nos. 0035/2019/A1 and SKL-IOTSC (UM)-2021-2023) and National Natural Science Foundation of China (Grant No. 52022001) are gratefully acknowledged.

NOTATION

A cross-sectional area of sand in large-diameter cylinder (m^2)

c_v consolidation coefficient of the bentonite slurry (m^2/s)

401 d hydraulic pore diameter (m)

402 d_{10} grain diameter for which 10% is finer than (mm)

403 d_s mean diameter of sand (m)

404 D_1, D_2 diameter of the large cylinder and small cylinder, respectively (m)

405 i hydraulic gradient

406 k_b hydraulic conductivity of sand for bentonite slurry (m/s)

407 k_s hydraulic conductivity of sand for water (m/s)

408 L maximum infiltration distance (m)

409 L_s equivalent length of sand column (m)

410 L_{s1} length of sand column in the large cylinder (m)

411 L_{s2} length of sand column in the small cylinder (m)

412 n porosity of saturated sand

413 Pe Peclet number

414 Q discharge (m^3)

415 t time (s)

416 v_p pore fluid velocity (m/s)

417 V water volume discharged from the sand column (m^3)

418 x infiltration distance at any time (m)

α fitting factor ($2 \leq \alpha \leq 4$)

γ_s specific weight of sand particle (N/m^3)

γ_b specific weight of bentonite slurry (N/m^3)

φ_0 piezometric head in the slurry (m)

τ_f yield strength of fluid (Pa)

τ_y yield strength of slurry (Pa)

Δp pressure drop over sand column (Pa)

$\Delta p'$ pressure drop between two adjacent PPTs (Pa)

$\Delta \varphi$ piezometric head in bentonite slurry (m)

REFERENCES

API (American Petroleum Institute) (2003). Recommended practice standard procedure for field testing water-based drilling fluids, 13B–1, 3rd edn. Washington, DC, USA: American Petroleum Institute.

Bezuijen, A. (2019). Keynote Lecture: Soil-water-tunnel interaction at the front face of a TBM. In Proceedings of 4th International Conference on Geotechnics for Sustainable Infrastructure Development (eds D. L. Phung and D. Nguyen), pp. 207–220. Hanoi, Singapore: Springer.

COB (Centre for Underground Construction) (2000). Second Heinenoord tunnel evaluation report, COB report K100-06. Gouda, the Netherlands: COB.

438 Fritz, P. (2007). Additives for slurry shields in highly permeable ground. *Rock Mechanics and*
439 *Rock Engineering*, 40 (1), 81–95.

440 Krause, T. (1987). Schildvortrieb mit flüssigkeits- und erdgestützter Ortsbrust. PhD thesis,
441 Technischen Universität Carolo-Wilhelmina, Braunschweig, Germany (in German).

442 Min, F. L., Du, J. R., Zhang, N., Chen, X. G., Lv, H. J., Liu, L. C. & Yu, C. J. (2019).
443 Experimental study on property change of slurry and filter cake of slurry shield under
444 seawater intrusion. *Tunnelling and Underground Space Technology*, 88, 290–299.

445 Min, F. L., Zhu, W. & Han, X. R. (2013). Filter cake formation for slurry shield tunnelling in
446 highly permeable sand. *Tunnelling and Underground Space Technology*, 38, 423–430.

447 Steeneken, S. P. (2016). Excess pore pressures near a slurry tunnel boring machine modelling
448 and measurements. Master thesis, Delft University of Technology, Delft, the Netherlands.

449 Talmon, A. M., Mastbergen, D. R. & Huisman, M. (2013). Invasion of pressurized clay
450 suspensions into granular soil. J. Porous Media 16, No. 4, 351–365.

451 Xu, T. & Bezuijen, A. (2019a). Pressure infiltration characteristics of bentonite slurry.
452 *Géotechnique*, 69 (4), 364–368.

453 Xu, T. & Bezuijen, A. (2019b). Bentonite slurry infiltration into sand: filter cake formation
454 under various conditions. *Géotechnique*, 69 (12), 1095–1106.

455 Xu, T. & Bezuijen, A. (2019c). Experimental study on the mechanisms of bentonite slurry
456 penetration in front of a slurry TBM. *Tunnelling and Underground Space Technology*, 93,
457 103052.

458 Yin, X. S., Chen, R. P., Li, Y. C. & Qi, S. (2016). A column system for modelling bentonite
459 slurry infiltration in sands. Journal of Zhejiang University–Science A (Applied Physics &
460 Engineering), 17 (10), 818–827.

461 Zhu, W., Qian, Y. J., Min, F. L., Wang, L., Wang, C., Xu, C. & Wang, J. N. (2019). Current
462 status and some problems of slurry shield in China. Tunnel Construction, 39 (5), 724–735
463 (in Chinese).

464 Zizka, Z. (2019). Stability of slurry supported tunnel face considering the transient support
465 mechanism during excavation in non-cohesive soil. Doctoral thesis, Ruhr University
466 Bochum, Bochum, Germany.

467 Zizka, Z., Schoesser, B., Thewes, M. & Schanz, T. (2019). Slurry shield tunneling: new
468 methodology for simplified prediction of increased pore pressures resulting from slurry
469 infiltration at the tunnel face under cyclic excavation processes. International Journal of
470 Civil Engineering, 17, 113–130.